Published in final edited form as:
JACC Cardiovasc Imaging. 2010 November ; 3(11): 1158–1165. doi:10.1016/j.jcmg.2010.08.014.

Towards Real-Time Intravascular Endoscopic Magnetic Resonance Imaging

Shashank Sathyanarayana, PhD[*], **Michael Schär, PhD**[*,†], **Dara L. Kraitchman, VMD, PhD**[*], and **Paul A. Bottomley, PhD**[*]

[*] Division of MR Research, Department of Radiology, and Department of Electrical and Computer Engineering, Johns Hopkins University, Baltimore, Maryland [†] Philips Healthcare, Cleveland, Ohio

Abstract

Fast, minimally invasive, high-resolution intravascular imaging is essential for identifying vascular pathological features and for developing novel diagnostic tools and treatments. Intravascular magnetic resonance imaging (MRI) with active internal probes offers high sensitivity to pathological features without ionizing radiation or the limited luminal views of conventional X-rays, but has been unable to provide a high-speed, high-resolution, endoscopic view. Herein, real-time MRI endoscopy is introduced for performing MRI from a viewpoint intrinsically locked to a miniature active, internal transmitter–receiver in a clinical 3.0-TMRI scanner. Real-time MRI endoscopy at up to 2 frames/s depicts vascular wall morphological features, atherosclerosis, and calcification at 80 to 300 μm resolution during probe advancement through diseased human iliac artery specimens and atherosclerotic rabbit aortas in vivo. MRI endoscopy offers the potential for fast, minimally invasive, transluminal, high-resolution imaging of vascular disease on a common clinical platform suitable for evaluating and targeting atherosclerosis in both experimental and clinical settings.

Keywords

atherosclerosis; calcium; endoscopy; intravascular; magnetic resonance imaging

Millions of cardiac catheterizations are performed annually in the U.S. to diagnose and treat cardiovascular disease. Advanced atherosclerosis is marked by the presence of lesions with high extracellular lipid and thin fibrous caps that are prone to rupture with potentially dire consequences (1). Although X-ray fluoroscopy with intravascular contrast agents is routinely used for guiding catheterization procedures, only the lumen is highlighted, limiting the ability to identify potentially significant lesions for diagnosis or targeted transluminal therapy. In addition, both the patient and interventionalist are exposed to ionizing radiation. Intravascular ultrasound imaging is a non-ionizing alternative, but does not have the spatial resolution or contrast of X-ray, especially when calcification is present. Magnetic resonance

Reprint requests and correspondence: Dr. Paul A. Bottomley, Division of MR Research, Department of Radiology, Johns Hopkins University, Park Building 310, 600 North Wolfe Street, Baltimore, Maryland 21287. bottoml@mri.jhu.edu.
Drs. Sathyanarayana and Schär are currently full-time employees of GE Healthcare, Bangalore, India, and Philips Healthcare, respectively. Dr. Sathyanarayana was a graduate student trainee and not a GE employee at the time of the work. Dr. Schär is a Visiting Scientist at Johns Hopkins University. Drs. Bottomley and Sathyanarayana are coinventors of a patent on the technology filed by Johns Hopkins University and licensed to SurgiVision, Inc., a Johns Hopkins University start-up company with which Dr. Bottomley has a financial relationship that is managed in accordance with the University's conflict-of-interest policies. Drs. Schär and Kraitchman report that they have no relationships to disclose.

imaging (MRI) offers intrinsically high soft-tissue contrast and multifunctional capabilities without ionizing radiation and may prove ideal for high-resolution targeted diagnostics and intervention (2) if its spatial resolution and speed could be improved.

The speed and spatial resolution of MRI depend critically on the signal-to-noise ratio (SNR), which can be improved with higher magnetic field strengths, smaller detectors (3), efficient MRI pulse sequences, or a combination thereof. Although not mutually exclusive, achieving all 3 simultaneously can present significant hurdles. For example, miniaturizing the detector to the size of an intravascular catheter or guidewire can permit internal MRI at submillimeter resolution, but not yet with both high-resolution and real-time acquisition (2–5). Increasing MRI's main magnetic field strength, B_0, to improve SNR and speed risks potentially unsafe device heating from the radiofrequency (RF) excitation field (3). Recently, it was shown that for internal detectors, an approximately B_0^2 improvement in the SNR of internal detectors can be realized and that heating can be controlled by switching the device off (3) or using it both to transmit and to receive (4).

Traditionally, MRI is locked to the frame of reference of the MRI scanner, thus requiring a seek-and-find imaging strategy to locate an internal probe. However, MRI localization that is intrinsic to the miniature internal detector itself is now possible by modifying the internal probe's sensitivity to achieve a thin sensitive disk near the tip, perpendicular to the probe's long axis (4). This avoids seek-and-find routines and provides efficient image acquisition of high SNR directly from the viewpoint of the device. The approach is analogous to imaging with a conventional optical endoscope, except that one potentially can see through the surrounding vessel and soft tissue with all of the standard MRI tools for enhancing contrast and probing function. Even so, the scan times of minutes per frame demonstrated in initial MRI endoscopy studies (4) were not conducive to conventional endoscopic procedures.

Herein, we introduce an MRI endoscopy approach with an approximately 100-fold reduction in scan time, providing real-time intravascular imaging from the probe's viewpoint as it is advanced into a vessel at several frames per second and 300-μm resolution. The protocol can be combined with 80-μm resolution imaging of vessel walls to identify suspect lesions and potentially target them for intervention. Feasibility is demonstrated in vitro with 2- to 3-mm diameter devices in atherosclerotic human iliac specimens and in a rabbit model of atherosclerosis studied in vivo on a standard clinical 3.0-T whole-body MRI scanner. The technology, which involves a combination of hardware, MRI pulse sequence, and post-processing software advances, is potentially applicable to the diagnosis of vascular disease, and the experimental evaluation of targeted image-guided intervention in translational research settings.

The hardware comprises an MRI endoscopy probe (4), which for our in vitro studies were fabricated with 4 3-mm outer diameter (OD) turns of 0.3-mm OD insulated copper wire and were tuned to resonate at a 128 MHz MRI frequency (with a 51-pF nonmagnetic 1.7-mm ceramic chip capacitor) (Fig. 1A). The coils were mounted at the end of a 40-cm (quarter wavelength, $\lambda/4$) 2.8-mm diameter UT-85C semirigid copper coaxial cable and insulated using polyester heat-shrink tubing (Advanced Polymers, Salem, New Hampshire). The cable is connected to an impedance matching network described previously (4) and is interfaced to a Philips 3.0-T Achieva MRI scanner (Philips Healthcare, Cleveland, Ohio).

For in vivo intravascular MRI endoscopy, 5-turn 2.3-mm maximum OD loop endoscopes were built, tuned (91-pF capacitor), and mounted on 59-cm lengths of 0.8-mm OD biocompatible nitinol coaxial cable (Nitinol Devices and Components, Fremont, California). The nitinol cable in turn was connected to a 64-cm 1.29-mm OD miniature flexible coaxial cable (K0115207, Huber-Suhner, Pfaffikon, Switzerland) to isolate the torque applied during

probe insertion from the matching circuit. Together, the nitinol and flexible cables form a tuned $3\lambda/4$ transmission line. During conventional MRI transmission from the scanner's body or head coils (but not during MRI endoscopy), the tuned cable and 5-turn detector at its distal end are shut off and decoupled by means of a blocking diode in the matching circuit as described previously (3,4).

The MRI endoscopy method uses the probe for both MRI transmission and reception (4). The MRI sensitivity of probes immersed in 0.35% saline (density, 1 g/ml; conductivity, ρ = 0.65 S/m; dielectric constant, ε_r = 80, comparable with skeletal muscle at 128 MHz) was computed using a full-wave electromagnetic method-of-moment analysis (FEKO, EM Software and Systems, Stellenbosch, South Africa). The coaxial cable was modeled as a 0.25-mm OD inner conductor with a polytetrafluoroethylene dielectric (ε_r = 2.2; loss-tangent, tanδ = 0.0002) and a 2.8-mm OD outer conducting shield. The probes were excited with adiabatic MRI pulses to enhance localization and adjusted to provide a uniform flip angle (FA) for radii $r \leq 7$ mm from the probe center (Fig. 1) (4). This requires just 2.2 W of RF power (vs. 10 to 30 kW for conventional whole body MRI), which limits local heating to ≤1°C during MRI endoscopy studies (4).

The combination of adiabatic excitation and the detector's limited sensitivity produces a thin sensitive disk perpendicular to the cable and centered on the detector, with a substantially uniform FA therein. The sensitivity profile with the lead oriented parallel to B_0 (and z-axis) is plotted in Figure 1A. It includes a frontal lobe that accounts for approximately 9% of the total sensitivity. Although relatively small, this lobe provides a modest forward-looking capability inasmuch as the center of the sensitive disk, being occupied by the detector and cable, contribute no MRI signal. If the distance between the probe tip and the center of the coil is short, the observed signal derives primarily from the integrated signal beyond the probe tip, which fades rapidly with distance and is dominated by the initial few millimeters (Fig. 1A). This feature is illustrated in images from a human iliac artery specimen, which show an arterial bifurcation as confirmed by coronal MRI performed with the scanner's 3.0-T (FLEX-M) surface coil (Figs. 1C and 1D). The full-width half-maximum thickness of the sensitive disk obtained by integrating the sensitivity profile (Fig. 1A) along the z-axis increases from 1.5 mm at the probe surface to 4 mm for radii extending to 3% of the maximum sensitivity (4).

With 1 dimension intrinsically localized along the z-axis using the above transmit–receive mechanisms (Fig. 1A), conventional MRI slice selection is omitted for real-time endoscopy. Conventional MRI gradients then are applied to localize the signals within the 2 dimensions of the sensitive disk (4). The time required to image the disk depends directly on the number of MRI phase-encoding steps, which is proportional to the field of view (FOV) and spatial resolution within the plane of the sensitive disk. However, the sensitivity within the disk decreases rapidly with r, limiting the effective FOV to $r \leq 15$ mm. Consequently, a reduced number of phase encodes suffices to avoid alias artifacts, enabling substantial scan time reductions for real-time endoscopy as compared with conventional MRI performed with much larger FOVs.

Two different protocols were developed for high-speed and for higher-resolution MRI endoscopy. Real-time endoscopy was performed with a 2-dimensional balanced steady-state free-precession sequence in which slice-selection is replaced by adiabatic RF pulses (duration, 2 ms; frequency sweep, ± 40 kHz; FA = 90°; threshold RF field of B_1 = 30 μT), 50 phase-encoding steps, and 300-μm in-plane resolution in 0.4- to 1-s scan times (repetition time, 8 to 12 ms). For high-resolution MRI endoscopy, a cardiac-gated 3-dimensional gradient-echo sequence with ≤10 phase encodes on the z-axis was used to increase the

resolution along the probe axis while avoiding banding artifacts (8 ms adiabatic pulses; frequency sweep, ±15 kHz; FA = 50°; threshold $B_1 = 10\mu T$; repetition time, 300 ms).

To improve image visualization during real-time studies, 3 post-processing tools were implemented. The first addressed the effect of probe orientation on the spatial encoding of the sensitive disk by the MRI scanner gradients. When the probe's long axis is parallel to the z-axis, gradient encoding is applied in the transverse, x-axis and y-axis directions. When vessels deviate from the z-axis, there is some SNR loss (≤15% for angles $\theta \leq 30°$ relative to the z-axis), and partial volume effects can cause blurring of off-axis structures depending on sample anatomic features, resolution, and probe orientation (4). To ameliorate partial volume effects, the orientation of the encoding plane was occasionally updated by determining the probe position via a user-initiated projection sequence programmed into the scanner's real-time user interface. For this, readout MRI gradients were applied without slice selection on the 3 gradient axes (total time, 20 to 30 ms), and the coil position was computed from the 3 projections. Successive coil positions were used to compute new in-plane gradient orientations perpendicular to the position vector joining consecutive coil positions and were fed back to the scanner for the next image acquisition. The orientation is updated when image blurring resulting from the probe being askew appears detrimental. The successive coil positions also are used to map the trajectory of the endoscope.

Second, a normalized cross-correlation algorithm was applied to provide a continuous image stream from the probe's viewpoint by translating the images to the (fixed) center of the FOV. Planar images generated during MRI endoscopy are characterized by intense local signals whose position in the FOV depends on the location of the device in the MRI plane, which moves as the probe is advanced. Normalized cross-correlation is routinely used in image processing to identify a pattern within an image based on a template of the pattern being sought. The template is moved across the image FOV and the normalized cross-correlation is computed at each location. This is highest when the template and pattern are aligned. In high-speed MRI endoscopy, successive images are more-or-less similar in appearance because they arise from closely spaced sample locations. Thus, each image is used as the algorithm's template to align the next image in the stream. This was implemented in MATLAB (Mathworks, Natick, Massachusetts; subroutine, normxcorr2). Excessive image blur can affect alignment, occasionally causing an image in the cine stream to jump.

Third, because the highly nonuniform, approximately 1/r, sensitivity dependence of miniaturized internal detectors can obscure local morphologicical features when visualized with standard linear displays, a simple correction that weighted the image intensity with distance from the center of the detector was applied. The device center was prescribed in one image, and the intensity correction automatically applied to the entire aligned image stream.

The SNR performance in arteries was measured from endoscopic images and also from surface-coil images acquired using identical scan parameters for comparison. The SNR was calculated as the ratio of the mean (uncorrected) image intensity to the standard deviation of the noise measured in separate images acquired with the gradients and RF transmitter turned off. The endoscope's SNR was corrected for the variable slice width using computed values reported elsewhere (4).

In vitro studies were performed on fresh human iliac tissue specimens obtained from the autopsy service of the authors' institution. Specimens were mounted on an acrylic support and were immersed in a saline bath. A scout scan was performed with the scanner's 3.0-T FLEX-M surface coil, followed by second-order volume shimming. The in vitro MRI

endoscope was encapsulated in a balloon and advanced into the vessel while recording endoscopic images using the high-speed imaging protocol. The images were displayed in real time on the scanner and were stored. Probe advancement was paused when the operator identified a suspect atherosclerotic lesion, the real-time mode was exited, and high-resolution imaging was performed. After MRI, the specimen was sectioned at the suspect site, fixed in 4% paraformaldehyde, and embedded in paraffin wax. X-ray computed tomography (CT) was performed on the paraffin-wax block (Gamma Medica-Ideas, Northridge, California) to demonstrate the presence of calcification. Histological sections obtained from the same block underwent von Kossa staining to detect calcium phosphate deposition.

All animal studies were approved by our Institutional Animal Care and Use Committee. In vivo studies were performed on 2 healthy male New Zealand white rabbits and 4 female Watanabe heritable hyperlipidemic rabbits in which atherosclerotic lesions develop spontaneously. Rabbits were sedated with intramuscular acepromazine (1 mg/kg) and ketamine (40 mg/kg), induced with intravenous sodium thiopental, and intubated to maintain an open airway. Before MRI, X-ray c-arm CT was performed after an intravenous injection of iodinated contrast agent (ioxehol, GE Healthcare; 2 ml/s for 8 s), using a standard digital subtraction angiography preset (Siemens Axiom Artis dFA DynaCT, Siemens Medical Solutions, Forchheim, Germany; rotation, 8 s; 240° scan angle; 0.5° increment; 0.36-μGy dose/pulse). Projection images were reconstructed into axial cross-sectional images (Siemens Syngo Inspace reconstruction algorithm, XLeo workstation, Siemens Medical Solutions). A nitinol MRI endoscope was then inserted into the descending aorta via a surgical cut-down just inferior to the renal arteries, and the animal was moved to the MRI scanner. Scout MRI and second-order volume shimming were performed while engaging the blocking diode in the antenna's matching circuit for conventional MRI. The blocking diode was switched open, and the probe was advanced into the aorta while recording high-speed endoscopic images. High-resolution imaging was performed at suspect sites in the vessel, noting their locations relative to the iliac bifurcation on the scout image for subsequent matching to histopathologic images.

After MRI, animals were sacrificed humanely. The aortic and iliac arteries traversed by the MRI endoscope were harvested and examined grossly for thermal injury, which typically manifests as tissue necrosis in acute studies. The tissue samples were sectioned at the suspect locations identified by MRI, fixed in 4% paraformaldehyde, and embedded in paraffin, and the sections were stained (Verhoeffvan Gieson) to highlight nuclei, collagen, connective tissue, and fibrin for correlation with MRI scans.

Figure 2 shows a series of real-time image frames extracted from a data stream recorded during advancement of an MRI endoscope at 1 frame/s through a diseased, intact, fresh, human iliac artery specimen immersed in a saline bath. Calcifications in atherosclerotic lesions in the vessel wall appear as dark patches, confirmed by von Kossa staining and by micro-CT of corresponding sections of the vessel obtained after MRI (Figs. 2E, 2F, and 2G).

Several in vivo image frames recorded from a rabbit aorta using the in vivo nitinol MRI endoscope are depicted in Figure 3. To track its advancement relative to the gross anatomic features in the laboratory frame of reference (Fig. 3A), the MRI endoscope was operated in receive-only mode (blocking-diode engaged), and its signal was combined with that of the scanner's standard FLEX-M surface coil (Fig. 3A). By itself, the SNR provided by the external surface coil is inadequate for high-resolution imaging of the vessel, although it is but a few centimeters away in this animal model (Fig. 3B). The measured SNR of the endoscope is 20-fold higher than that of the product surface coil at the vessel wall (r = 2

mm) (Fig. 3C) but is less than that of the surface coil SNR at larger distances from the endoscope.

Real-time in vivo MRI endoscopy at 2 frames/s with the scanner's detection coils turned off reveals the lumen (Fig. 3C) and a suspected aortic lesion in a Watanabe heritable hyperlipidemic rabbit atherosclerosis model (Fig. 3D) during device advancement through the aorta. The lesion is confirmed by higher-resolution (80 μm) endoscopic MRI in vivo (Fig. 3E) and by postmortem histological examination, which shows the intima and 2 small lesions (Fig. 3F, arrows). The c-arm CT of the same animal obtained before MRI endoscopy showed an irregularly shaped aorta at the location of the lesion, but failed to detect the plaque seen by MRI endoscopy (Figs. 3G and 3H). Verhoeff-Van Gieson staining of histological specimens showed the disrupted collagen architecture of the plaque, but neither gross examination of vessels nor the histological examination showed any evidence of heat injury or plaque rupture from the endoscope in the regions traversed. The cine video streams corresponding to Figures 2 and 3 are available online (Online Videos 1, 2, and 3).

MRI endoscopy is a novel technology that uses a combination of internal probe design, MRI excitation sequencing, and post-processing to provide high-resolution MRI from a viewpoint intrinsically locked to the distal end of an internal probe. Herein, we have introduced and demonstrated for the first time that MRI endoscopy can provide a probe's-eye view of intravascular morphological and pathological features in real time at 1 to 2 frames/s and 300-μm in-plane resolution. This is approximately 2 orders of magnitude faster than our earlier work (4), primarily the result of advances in the endoscopic MRI method. Higher-resolution imaging as fine as 80 μm was then possible in targets of interest in vivo (Fig. 3E). Use of superelastic nitinol for the in vivo probe shafts affords them torque and maneuverability, analogous to that of conventional intravascular nitinol guidewires. The limited range of the MRI endoscope's excitation field limits the net power deposited in the sample, as well as excitation of extraneous signals.

The present studies benefit from an intrinsic increase of nearly 4-fold in SNR for miniature internal MRI detectors operating in the newer clinical 3.0-T MRI scanners, as compared with the older 1.5-T units (3). MRI endoscopy at 1.5-T also should be practical with the methods described, the detrimental affects of the lower SNR notwithstanding (e.g., an approximately 4-fold in-plane reduction in spatial resolution or an approximately 16-fold increase in scan time, all else being unchanged). Conversely, even higher SNR may be possible with the development of human 7.0-T MRI systems, if safety issues can be addressed.

A real-time intravascular MRI endoscope with a limited forward-viewing capability to reduce the risk of mechanical injury, plaque rupture, or emboli, may serve as a guidewire to introduce diagnostic or therapy delivery catheters. Indeed, in the present in vivo and in vitro studies, the MRI endoscopes were advanced without guidance by any other imaging method, including conventional MRI. The device size was essentially determined by the endoscopic coil OD, the reduction of which, however, deleteriously affects the range or FOV of the device. A smaller loopless antenna-based endoscope design with a diameter comparable with the nitinol cable from which it is formed (e.g., approximately 1 mm) may be preferable in applications requiring smaller OD devices for use as guidewires (4).

Although a direct comparison of MRI endoscopy with intravascular ultrasound has not been carried out, intravascular ultrasound typically is performed during withdrawal of an imaging catheter threaded over a guidewire already inserted under X-ray fluoroscopic guidance, but is faster than the MRI endoscopy frame rate demonstrated here. MRI is not confounded by diffraction or reflection artifacts from calcifications (2), and its contrast can be optimized for

the characteristic properties of the target pathological features (5). Like conventional optical endoscopy, access to other vessels—the esophagus, stomach, urinary tract, colon, bronchial passages, and so forth—also should be feasible for millimeter-sized MRI endoscopes to provide high-resolution transmural imaging from the probe's viewpoint, with the high soft-tissue contrast afforded by MRI. Further work will be needed to determine its role in the context of existing techniques and imaging tools.

The MRI endoscopes tested here in diseased human specimens and in a rabbit atherosclerosis model in vivo provided definition of the vessel wall and permitted identification of lesions, including calcifications whose measurement by cardiovascular X-ray CT is useful for assessing plaque burden in patients at risk for coronary heart disease. Indeed, the rabbit aorta is comparable in size with human coronary vessels (3 to 4 mm), and the present study was performed on a commercial clinical 3.0-T MRI scanner that is widely available for routine patient studies, and not on an ultrahigh-field MRI system typically used for small animals. Thus, MRI endoscopy may provide a fast, high-resolution, transluminal assessment of pathological features in human-sized vessels on a common imaging platform that is suitable for translational research from animal models to clinical trials in humans.

Supplementary Material

Refer to Web version on PubMed Central for supplementary material.

Acknowledgments

The authors thank Meiyappan Solaiyappan for advice and assistance with the algorithm used for centering real-time images and Dr. Barbara Crain and the Johns Hopkins Hospital Autopsy Service for supplying pathological specimens.

This work was supported by National Institutes of Health grants R01 EB007829 and R01 HL090728 (to Dr. Bottomley), and R21/R33HL89029 (to Dr. Kraitchman).

ABBREVIATIONS AND ACRONYMS

CT	computed tomography
FA	μflip angle
FOV	μfield of view
MRI	magnetic resonance imaging
OD	outer diameter
RF	radiofrequency
SNR	signal-to-noise ratio

References

1. Stary HC, Chandler AB, Dinsmore RE, et al. A definition of advanced types of atherosclerotic lesions and a histologic classification of atherosclerosis. A report from the Committee on Vascular Lesions of the Council on Arteriosclerosis, American Heart Association. Circulation. 1995; 92:1355–74. [PubMed: 7648691]
2. Meissner OA, Rieger J, Rieber J, et al. High-resolution MR imaging of human atherosclerotic femoral arteries in vivo: validation with intravascular ultrasound. J Vasc Interv Radiol. 2004; 14:227–31. [PubMed: 12582191]
3. El-Sharkawy AM, Qian D, Bottomley PA. The performance of interventional loopless MRI antennae at higher magnetic field strengths. Med Phys. 2008; 35:1995–2006. [PubMed: 18561676]

4. Sathyanarayana S, Bottomley PA. MRI endoscopy using intrinsically localized probes. Med Phys. 2009; 36:908–19. [PubMed: 19378751]
5. Larose E, Yeghiazarians Y, Libby P, et al. Characterization of human atherosclerotic plaques by intravascular magnetic resonance imaging. Circulation. 2005; 112:2324–31. [PubMed: 16203910]

APPENDIX

For supplementary videos and their legends, please see the online version of this article.

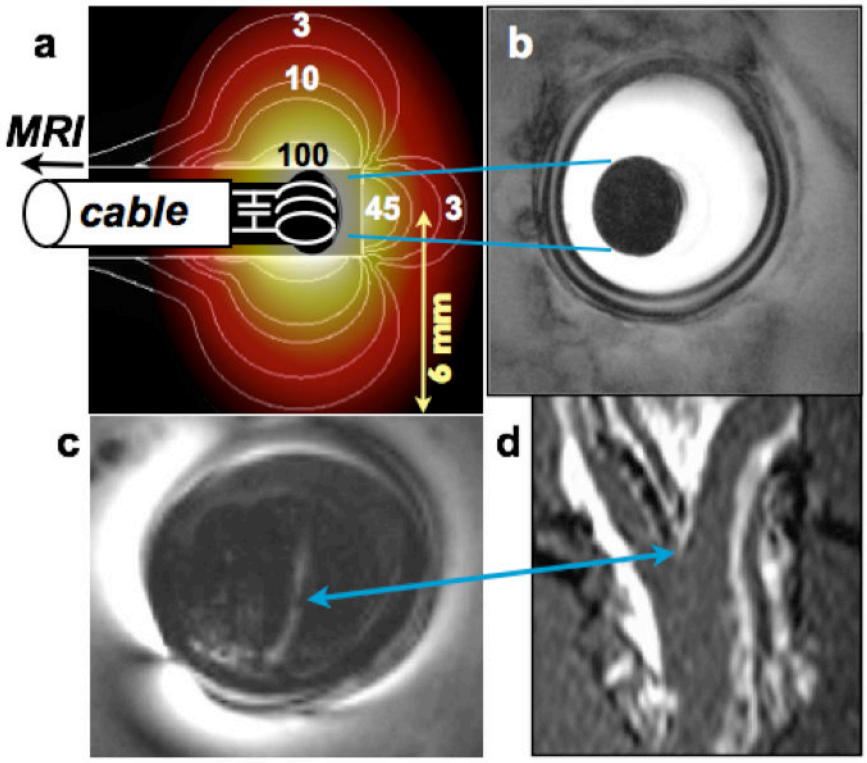

Figure 1. Spatial Localization With Endoscopic MRI

(A) Computed (electromagnetic method-of-moments) MRI sensitivity (contours overlaid with color shading, normalized to 100 at the coil edge) of loop endoscope in 0.35% saline. Adiabatic excitation provides a uniform flip angle for radii $r \leq 7$ mm. The sensitivity contours illustrate intrinsic localization perpendicular to the cable axis. The full-width-half-maximum thickness of the profile is given by the integral of the signal along the cable z-axis (4). **(Inset)** Photograph of the cable end, tuning capacitor, and looped endoscope (same scale). **(B)** In vitro endoscopic image from a porcine aorta (in-plane resolution, 100 μm; scan time, 100 s; 2-dimensional GRE; TR = 0.5 s; TE = 20 ms). **(C)** The modest forward-looking capability of a short-tip endoscopic probe detects a bifurcation in a human iliac artery specimen (TR/TE = 500/20 ms; FA = 20°; resolution, 100 μm), evident in a corresponding surface coil coronal MRI: (**D**) 3-dimensional GRE; TR/TE = 9/2 ms; FA = 30°. No MRI slice selection is used in **(B)** or **(C)**. FA = flip angle; GRE = gradient echo; MRI = magnetic resonance imaging; TE = echo time; TR = repetition time.

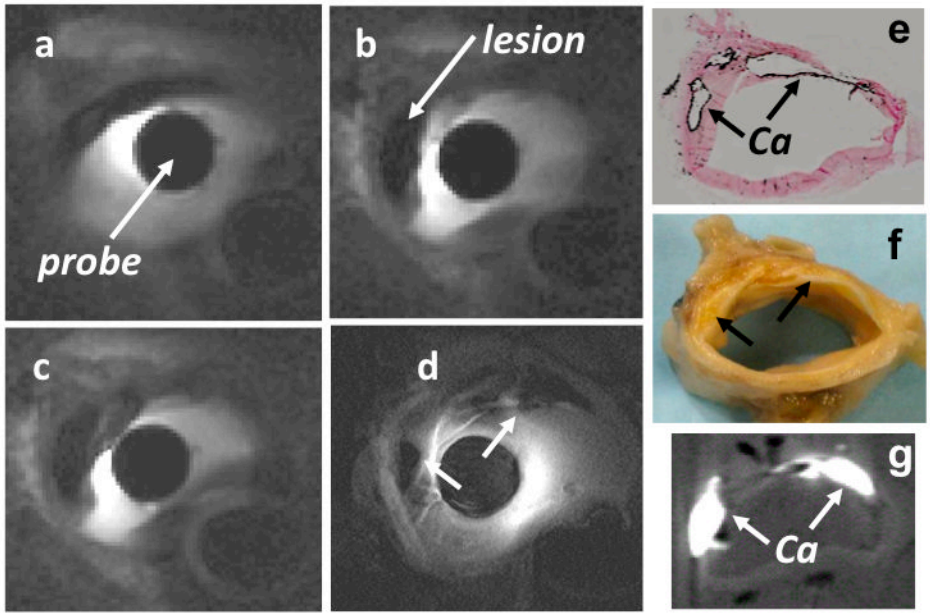

Figure 2. Real-Time MRI Endoscopy in Iliac Artery Specimens

(A to C) MRI endoscopy images obtained from a sequence acquired at 1 frame/s from a diseased human iliac artery sample in vitro (2-dimensional balanced steady-state free-precession sequence; TR/TE = 12/6 ms; FA = 90°; 300 μm in-plane resolution). These and **(D)** higher-resolution (100 μm) endoscopic MRI show **(E)** calcifications (Ca) as **dark patches**, confirmed by von Kossa staining **(dark rim, arrows)** and **(G)** X-ray micro-computed tomography (in-plane resolution, 80 μm; 0.8 mm slice thickness) of **(F)** the specimen sectioned after MRI. See Online Video 1. Abbreviations as in Figure 1.

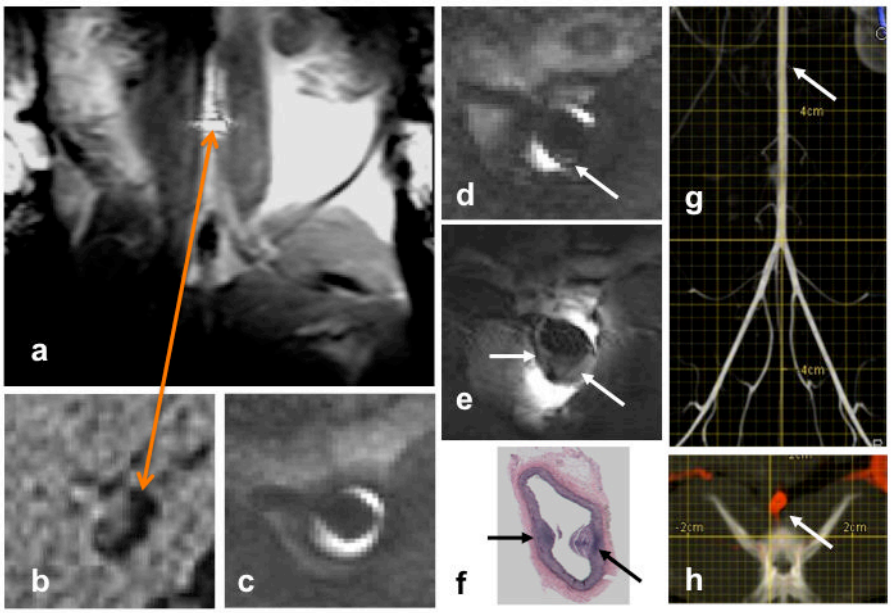

Figure 3. Real-Time In Vivo MRI Endoscopy in a Rabbit Aorta

(A) Image from a real-time series acquired from a rabbit aorta in vivo with the endoscope operating in receive-only mode and its signal combined with a standard 3.0-T (FLEX-M) surface coil, reveal its location **(bright disk, orange arrow)** relative to the gross anatomic features in the laboratory frame of reference. **(B)** High-resolution transverse image of the vessel with the external surface coil alone provides inadequate signal-to-noise ratio compared with 2 frames/s MRI endoscopy (2-dimensional balanced SSFP; TR/TE = 11/5 ms; FA = 90°; field of view shown, 10 mm; 300-μm in-plane resolution) in the aorta of a Watanabe heritable hyperlipidemic rabbit, **(C and D)** in vivo. A suspect lesion identified in **(D)** during advancement in the artery **(arrows)** is examined at higher resolution in **(E)** (3-dimensional GRE; TR/TE = 300/12 ms; in-plane resolution, 80 μm; 4.5 min/10 contiguous slices). **(F)** Lesions are confirmed in Verhoeff-van Gieson–stained sections of the vessel after death. **(G)** X-ray c-arm computed tomography (CT) reconstructed in the coronal plane from the subtracted portion of a flat-panel digital subtraction angiography scan acquired before MRI endoscopy in the same rabbit (scale, 2 mm/division). The lesion identified by MRI endoscopy is approximately 50 mm above the iliac bifurcation **(arrow). (H)** Axial c-arm CT with the subtracted angiographic portion displayed in **red** at the location of the lesion in **(G)** overlaid on the native image showing an irregularly shaped aorta **(arrow)**, but not the plaque. See Online Videos 2 and 3. SSFP = steady-state-free-precession sequence; other abbreviations as in Figure 1.